

Observation and mechanism of non-uniform distribution of tin nuclei in preparing vapor diffusion coated Nb₃Sn thin film for SRF applications*

Shuai Wu,^{1,2} Yang Ye,^{1,2} Zi-Qin Yang,^{1,2,3,†} Yuan He,^{1,2,3,‡} Jian-Peng Li,^{4,1} Guang-Ze Jiang,^{1,2} Lu Li,¹ Shi-Chun Huang,^{1,2} An-Dong Wu,^{1,2} Hang-Xu Li,^{1,2} Shao-Hua Lu,³ Tao Liu,¹ Feng Qiu,^{1,2} Cang-Long Wang,¹ Ji-Zheng Duan,¹ Teng Tan,^{1,2} Zhi-Jun Wang,^{1,2} Sheng-Hu Zhang,^{1,2} Hong-Wei Zhao,^{1,2} and Wen-Long Zhan^{1,2}

¹*Institute of Modern Physics, Chinese Academy of Sciences, Lanzhou 730000, China*

²*School of Nuclear Science and Technology, University of Chinese Academy of Sciences, Beijing 100049, China*

³*Advanced Energy Science and Technology Guangdong Laboratory, Huizhou 516007, China*

⁴*School of Microelectronics, Dalian University of Technology, Dalian 116000, China*

Growth of high-quality Nb₃Sn thin films for superconducting radiofrequency (SRF) applications using the vapor diffusion method requires a uniform distribution of tin nuclei on the niobium (Nb) surface. This study examines the mechanism underlying the observed non-uniform distribution of tin nuclei with tin chloride SnCl₂. Electron backscatter diffraction (EBSD) analysis was used to examine the correlation between the nucleation behavior and orientation of niobium grains in the substrate. The findings of the density functional theory (DFT) simulation are in good agreement with the experimental results, showing that the non-uniform distribution of tin nuclei is the result of the adsorption energy of SnCl₂ molecules by varied niobium grain orientations. Further analysis indicated that the surface roughness and grain size of niobium also played significant roles in the nucleation behavior. This study provides valuable insights into enhancing the surface pretreatment of niobium substrates during the growth of Nb₃Sn thin films using the vapor diffusion method.

Keywords: nucleation, tin chloride, non-uniform distribution, vapor diffusion, crystal orientation, adsorption energy

I. INTRODUCTION

Superconducting radio frequency (SRF) technology is the preferred technical approach for numerous accelerator projects that are currently being developed or are in the planning stage. These projects include the synchrotron radiation source such as the Shanghai synchrotron Radiation Facility project [1, 2], the high-energy colliders and attached high-energy experimental project, including the Circular Electron Positron (CEPC), Large Hardon Collider (LHC), and the Beijing Electron Positron Collider (BEPC/BES) [3–6], the free electron laser such as the Shanghai high-repetition-rate XFEL and extreme light facility (SHINE) [7–9], as well as the proton and heavy ion accelerator such as the High Intensity heavy-ion Accelerator Facility (HIAF) and the China initiative Accelerator Driven System (CiADS) [10–12]. SRF cavities play a crucial role in accelerating the charged particles in SRF accelerators. These cavities are commonly constructed using high-purity niobium with a residual resistivity ratio (RRR) exceeding 300. The performance of the Nb cavities in relation to both the maximum field and surface resistance [13, 14] is currently nearing its inherent limits. However, the typical operating temperature range for Nb cavities is approximately 2 K. The operation and maintenance expenses of large accelerators are significantly affected by the considerable size and complexity of cryogenic refrigerators as well as the significant power requirements of the electrical grid at this

temperature. To achieve cost reduction in the construction and operation of large-scale SRF accelerators, it is imperative to explore alternative materials that exhibit SRF performance beyond that of Nb.

In comparison to high-purity Nb utilized in accelerator applications, Nb₃Sn exhibits a higher theoretical superconducting transition temperature (T_c) of approximately 18.3 K (compared to approximately 9.25 K for Nb), a larger energy gap of approximately 340 mV (compared to approximately 140 mV for Nb), and a higher superheating magnetic field (H_{sh}) of approximately 425 mT (compared to approximately 240 mT for Nb) [15]. Hence, the Nb₃Sn thin-film SRF cavity can be operated at a temperature of 4.2 K or higher, thereby achieving a potential accelerating field twice as high as that of the Nb SRF cavity. The utilization of SRF technology is expected to have significant implications not only for major scientific facilities such as the International Linear Collider (ILC), but also for smaller research platforms such as compact light sources and photo-neutron sources. In addition, SRF technology shows promise for various industrial applications, including wastewater treatment and medical isotope production [16–19]. A crucial aspect of RF applications is the preparation of high-quality Nb₃Sn thin films on the inner side of the substrate cavity using suitable methodologies. Numerous techniques have been developed to fabricate Nb₃Sn thin films. For instance, S.K. Chen, E.A. Llyina, and W.W. Tan prepared Nb₃Sn thin films by magnetron sputtering [20–22], S. M. Deambrosio employed the liquid-tin dipping method to fabricate 6 GHz Nb₃Sn thin film cavities [23], and R.H. Hammond utilized electron beam co-evaporation to synthesize Nb₃Sn phases [24]. Furthermore, P.G. Kosky adopted chemical vapor deposition to prepare Nb₃Sn joints [25], M. Lu et al. studied the preparation of Nb₃Sn thin films through the bronze route [26–29], and S. Posen, U. Pudasaini and Z.Q. Yang conducted extensive research on the vapor diffu-

* This work was supported by the National Natural Science Foundation of China (No.12175283), Youth Innovation Promotion Association of Chinese Academy of Sciences (2020410) and Advanced Energy Science and Technology Guangdong Laboratory (HND20TDSPCD, HND22PTDZD).

† Corresponding author, yzq@impcas.ac.cn

‡ Corresponding author, hey@impcas.ac.cn

sion method [15, 30, 31]. In addition, other institutions have carried out relevant research on the preparation of Nb_3Sn thin films using the vapor diffusion method [32, 33]. Substantial advancements have been made in these methods over the past decade. Nevertheless, to date, the existing technique are not capable of generating cavities with superior performance compared to those produced using the vapor diffusion method [28, 31, 34, 35]. The presence of tin droplets on the surface and the occurrence of undesired tin-rich phases resulting from the liquid-tin-dipping approach contribute to the poor performance of Nb_3Sn cavities [23]. The prospective application of the Nb_3Sn thin film created using the bronze approach towards copper-based Nb_3Sn cavities is hindered by the probable contamination of the RF layer with residual copper. The Nb_3Sn SRF cavity, which involves the growth of a thin film of Nb_3Sn on the surface of an Nb cavity using the tin vapor diffusion process, has favorable characteristics, such as a high quality factor and a strong surface electromagnetic field [31–33]. Consequently, this technology has significant potential for various applications.

In the 1970s, researchers at Siemens AG attempted to fabricate high-frequency TE- and TM-mode Nb_3Sn cavities using vapor diffusion, a technique pioneered by Saur and Wurm [36]. They discovered that a nucleation period without special precautions was crucial to the occurrence of uncovered Nb spots in Nb_3Sn films. This challenge was successfully addressed by implementing an enhanced nucleation procedure. During the process, an oxide layer on the niobium cavity surface is initially cultivated via anodization, following which the temperature of the tin source is elevated to 200 °C above that of the substrate. Subsequently, B. Hiltenbrand discovered that the growth of high-quality Nb_3Sn films could be achieved by introducing a small quantity of tin halogenides, such as SnF_2 or SnCl_2 , into the coating chamber without the need to maintain the tin source temperature at 200 °C above the chamber temperature [37]. Studies conducted by Siemens demonstrated that nucleation is a crucial and essential process in the vapor diffusion method for the formation of Nb_3Sn films. During the initial stage of covering a thin-film SRF cavity with Nb_3Sn using the vapor-diffusion method, researchers at the University of Wuppertal employed nucleation conditions derived from investigations conducted by Siemens. The initial step involved anodizing the inner surface of the niobium cavity using a layer composed of Nb_2O_5 . Subsequently, a modest quantity of SnCl_2 evaporates at approximately 500 °C, leading to the formation of nucleation centers situated on the surface. At high temperatures, the Nb_2O_5 layer disintegrates, resulting in the absorption of oxygen by the niobium substrate. Consequently, the niobium surface is quickly brought into contact with the nucleation centers. However, a study conducted by the University of Wuppertal revealed that the anodization process for growing the Nb_2O_5 layer significantly reduces the RRR of the underlying niobium substrate which leads to a decrease in its thermal conductivity [38]. Consequently, in another study conducted by the University of Wuppertal, the coating of high-purity 1.5 GHz CEBAF-shaped Nb cavities conducted the nucleation process using SnCl_2 . This was observed specifically

for nonanodized surfaces without the requirement of maintaining the tin source temperature at 200 °C above that of the Nb cavity. In 2009, Cornell University restarted research on the vapor diffusion method for coating Nb_3Sn thin-film SRF cavities. This initiative has been driven by significant advancements and the near attainment of the theoretical limit for the performance of Nb SRF cavities. The initial nucleation technique employed at Cornell University maintained the SnCl_2 at 500 °C for 5 h after the degassing process. Subsequently, both the cavity and the tin heater were subjected to a gradual increase in temperature at an equivalent pace. In 2017, D. Hall from Cornell University modified the nucleation recipe to address the issue of inadequate tin coverage [39]. SnCl_2 was chosen as the nucleation agent; however, the tin source temperature was enhanced. Specifically, a layer of Nb_2O_5 was anodized on the inner surface of the substrate Nb cavity prior to coating. The deposition system utilized at the Jefferson Lab (JLab) lacks the capability to independently regulate the temperature of both the Nb cavity and the tin source. In the JLab coating procedure, nucleation sites are generated by subjecting SnCl_2 to a temperature of 500 °C for 1 h without anodization [40]. Furthermore, U. Pudasaini from JLab conducted a systematic investigation of the impact of several parameters, including the quantity of SnCl_2 , nucleation temperature, and nucleation duration, either individually or in combination. This study contributes significantly to the advancement of knowledge on nucleation [41]. Significant modifications were made to the nucleation step by S. Posen of the Fermi National Accelerator Laboratory (FNAL). In addition to employing SnCl_2 and anodization techniques, a notable divergence of this work lies in the elevated temperature range of the tin source during the nucleation stage, reaching as high as 1200–1250 degree. By implementing this alteration, the highest acceleration field of $24 \text{ MV} \cdot \text{m}^{-1}$ was achieved in a 1.3 GHz single-cell TESLA-shaped Nb_3Sn thin-film SRF cavity. This achievement was accompanied by a high Q_0 . The cavity was coated using the vapor diffusion approach, as documented in reference [42]. Numerous studies have examined the influence of nucleation on film growth during film preparation. These studies have consistently demonstrated that the nucleation behavior significantly affects both the growth and quality of the film [43–46]. The nucleation and growth mechanisms of the A15 phase have been studied in previous works [47–49]. However, relatively few studies have been conducted on the nucleation stage for the preparation of Nb_3Sn thin films using the vapor diffusion method [30, 50, 51].

As previously stated, nucleation plays a pivotal role and is a necessary condition for the successful development of a homogeneous and superior Nb_3Sn film using the vapor diffusion technique. Moreover, clarification of the nucleation process enables modification of the nucleation conditions, thereby improving the RF performance of the Nb_3Sn SRF cavity. This study examined the occurrence of a non-uniform distribution of tin nuclei on the surface of niobium during the nucleation stage. A correlation was established between the behavior of nucleation and grain orientation using EBSD characterization. Additionally, this study elucidates the underlying factors

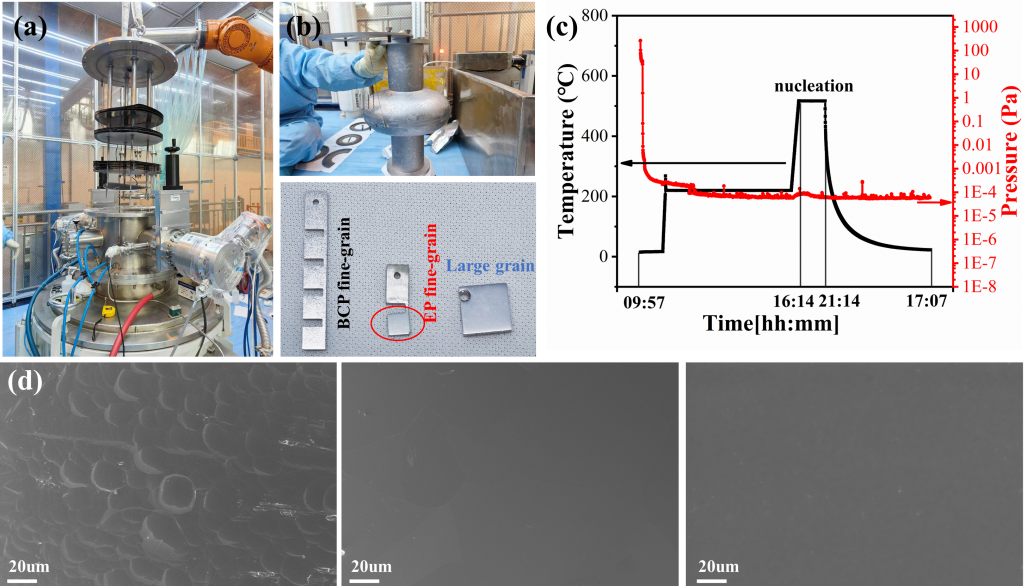


Fig. 1. (Color online) (a) Coating furnace for nucleation experiments, (b) nucleation samples include BCP fine-grain, EP fine-grain, and large-grain Nb, (c) temperature and pressure during the entire nucleation stage, (d) surface status of BCP fine-grain, EP fine-grain and BCP large grain Nb

that contribute to the non-uniform distribution of tin nuclei during the nucleation stage. The proposed mechanism is validated using simulation calculations. This study aims to improve our understanding of the nucleation process and offer insights into its optimization.

II. EXPERIMENTAL CHARACTERIZATION

A. Sample preparation

The Nb samples were obtained by wire-cutting a high-purity Nb sheet, which was utilized in the fabrication of cavities. The samples were subjected to identical treatment of SRF cavities, which involved the application of either 150 μm heavy BCP or EP, followed by annealing at a temperature of 800 $^{\circ}\text{C}$ for 3 h. In addition, a layer of 20 μm light BCP or EP was applied using standard electrolytes. After polishing, the samples were rinsed in a Micro-90 solution, followed by ultrasonic cleaning in ultrapure water for 30 min.

Nucleation experiments were conducted within the coating system employed for the fabrication of the Nb₃Sn thin-film cavities. The nucleation samples consisted of BCP fine-grain Nb samples, EP fine-grain Nb samples, and large-grain Nb samples. The purpose of these samples was primarily to confirm the significant correlation between the orientation and nucleation behavior in addition to elucidating the impact of various pretreatments on the nucleation behavior. The use of Nb samples with a larger grain size is aimed at providing a clearer representation of the correlation between nucleation behavior and grain orientation. Hence, the nucleation studies included large-grain materials chosen based on their distinct crystal orientations, as determined by XRD. The grain

size of these samples were approximately in the millimeter range. The initial pressure of the furnace before heating was superior to 5×10^{-5} Pa. The exact nucleation step consisted of a degassing stage lasting for 24 h, followed by a gradual increase in temperature at a rate of $3.5 \text{ }^{\circ}\text{C} \cdot \text{min}^{-1}$ until it reached 500 $^{\circ}\text{C}$. After maintaining the temperature for 4 h, it is recommended to cease the heating process and allow the furnace to cool down gradually. Notably, only SnCl₂ was employed as a source of tin vapor in the nucleation experiments. The coating furnace used for the nucleation experiments and the nucleation samples are shown in Fig. 1a and Fig. 1b. Temperature and pressure curves for the entire nucleation stage are shown in Fig. 1c. As shown, the surface of EP fine-grain is smooth, and the grain boundaries are clearly visible. Compared with EP fine-grain Nb, undulating features are heavily etched on the BCP fine-grain Nb surface, which results in a significantly higher surface roughness. Owing to the single surface orientation, the BCP LG Nb surface exhibits a high level of smoothness with no discernible grain boundaries. The specific morphologies are shown in Fig. 1d.

B. Characterization

Nucleation sites were examined using ZEISS Gemini 300 scanning electron microscopy (SEM) equipment, which was equipped with an energy dispersive X-ray spectroscopy (EDS) detector. A voltage of 15 kilovolts (kV) was used to accelerate the particles. X-ray diffraction (XRD) was used to examine the crystal structure of the niobium substrate. The analysis was conducted using an X'Pert PRO MPD diffractometer equipped with Cu K_α radiation at a wavelength of 1.5406 Å. The variation in tin content across

different crystal orientations was analyzed using Auger Electron Spectroscopy (AES) and Selected-Area X-ray Photoemission Spectroscopy (SAXPS). The AES analysis was conducted using a PHI 710 instrument employing a primary electron beam energy of 5 keV with a current of 10 nA. X-ray photoelectron spectroscopy (XPS) was conducted using a PHI 5000 Versaprobe 3 instrument equipped with an aluminum K_{α} source of radiation with an energy of 1486.6 electron volts (eV). The analysis chamber was maintained at a vacuum below 4.78×10^{-6} Pa. The correlation between the nucleation performance and grain orientation was investigated using an EBSD system connected to a field-emission SEM model, Quanta 200FEG, manufactured by FEI. The SEM was operated at an acceleration voltage of 20 kilovolts (kV). EBSD observations were conducted using a scanning step size of $0.2 \mu\text{m}$ within a scanning region of $0.5 \text{ mm} \times 0.5 \text{ mm}$, encompassing multiple grains. The data were processed using the OIMTSI software to obtain orientation maps with IPF coloring. Miller indices ($h \ k \ l$) corresponding to the exposed crystallographic planes were obtained and determined using the same software. It is important to highlight that, prior to conducting the nucleation experiment, it is necessary to eliminate the stress layer present on the surface of the sample while simultaneously guaranteeing minimal surface roughness.

C. Calculation model and method

The adsorption behavior of tin chloride on niobium surfaces with varying orientations was investigated using density functional theory (DFT) calculations. The crystal structure of niobium was acquired from its dedicated library, and the measured lattice constant of 3.03 \AA was in good agreement with the experimental value. Multiple $3 \times 3 \times 1$ niobium supercells were constructed, each with a distinct orientation. The periodic structures were simulated using slabs of six metal layers. To mitigate the potential contact between neighboring supercells, a vacuum layer with a thickness of approximately 15 \AA was implemented. The atomic positions of the adsorbates and the Nb layers were thoroughly optimized for each system, except for the atoms in the bottom three layers, which were fixed at their bulk positions. The tin chloride molecule was designed using the sketch-atom design tool. The bond length and angle were established at 2.363 \AA and 99° , respectively, and were aligned with the structure, as described in previous studies. Symmetry constraints were not utilized in the geometric optimization process, whereas spin polarization was incorporated in the calculations because of its significant impact on the energetics. The BFGS optimization procedure was employed by Broyden to decrease energy and achieve the most stable configuration of the computational model. The generalized gradient approximation (GGA) formulation and the Perdew-Burke Ernzerhof (PBE) functional were utilized to characterize the exchange between energy and potential. The interaction between the electron wave function and ion core was described using the OTFG pseudopotential hyper-soft potential. The precision of the SCF method was determined based on specific criteria. These criteria included

achieving a convergence of the single-atom energy to a value of 2.0×10^{-6} eV, ensuring that the force exerted on each atom was below $3.0 \times 10^{-2} \text{ eV} \cdot \text{nm}^{-1}$, and maintaining a tolerance for stress and displacement deviations of less than 0.05 GPa and 1.0×10^{-3} nm, respectively. The adsorption energies were determined through the subtraction of the energies associated with a SnCl_2 molecule in the gaseous phase (E_{SnCl_2}) and a clean Nb surface (E_{clean}) from the overall energy of the SnCl_2/Nb system ($E_{\text{SnCl}_2/\text{Nb}}$) which can be rewritten as $E_{\text{ads}} = E_{\text{SnCl}_2/\text{Nb}} - E_{\text{SnCl}_2} - E_{\text{clean}}$. Experiments were conducted on clean surfaces to evaluate the effects of variations in the cutoff energies and the number of k-points on the test calculations. The convergence of the cutoff energy was investigated with values ranging from 384 to 608 electron volts (eV). The k-point mesh was systematically adjusted from $2 \times 2 \times 1$ to $5 \times 5 \times 1$ to evaluate its effect on the results. The findings indicated that employing a cutoff energy of 480 eV in conjunction with a $3 \times 3 \times 1$ k-point mesh yielded sufficient levels of convergence.

III. RESULTS AND DISCUSSION

A. Non-uniform distribution of tin nuclei

The distribution of the tin nuclei in EP Nb samples is shown in the SEM images in Fig. 2. Fig. 2a shows the random distribution of bright and dark areas observed under low magnification following nucleation. Fig. 2b illustrates the observed topography of the boundary between the bright and dark regions. It is evident that the density and morphology of the tin particles in the two regions differ. Fig. 2c and Fig. 2d show high-magnification images illustrating the distribution of nuclear sites on the surface of the bright and dark areas, respectively. These images show significant variations in both the density and shape of the tin nuclei. EDS was used to measure the tin content, as depicted in Fig. 3, to confirm the observed differences in the tin nuclei density between the bright and dark areas in SEM images. The density of the tin nuclei differed substantially between the two regions, as shown in Fig. 3c, which depicts the results of the tin nuclei mapping. The EDS-measured tin contents in the dark and bright regions corresponding to Area 1 and Area 2 in Fig. 3a are summarized in Fig. 3d. The tin content in both regions is less than 10% because the tin nuclei on the surface have a thickness at the nanoscale level, whereas the detection depth of EDS is of the order of micrometers.

In Fig. 3a, the boundary between the two regions contains significantly more tin nuclei. From the EBSD results in III B we can conclude that this location represents the grain boundary which contains more defects and at which nucleation is more likely to occur.

Furthermore, a non-uniform distribution of tin nuclei was observed in a specific subset of BCP nucleation samples, as depicted in Fig. 4a. The observed variations in the nucleation behavior across different grain surfaces indicate a strong correlation between the nucleation density and grain orientation throughout the nucleation process. To examine the cor-

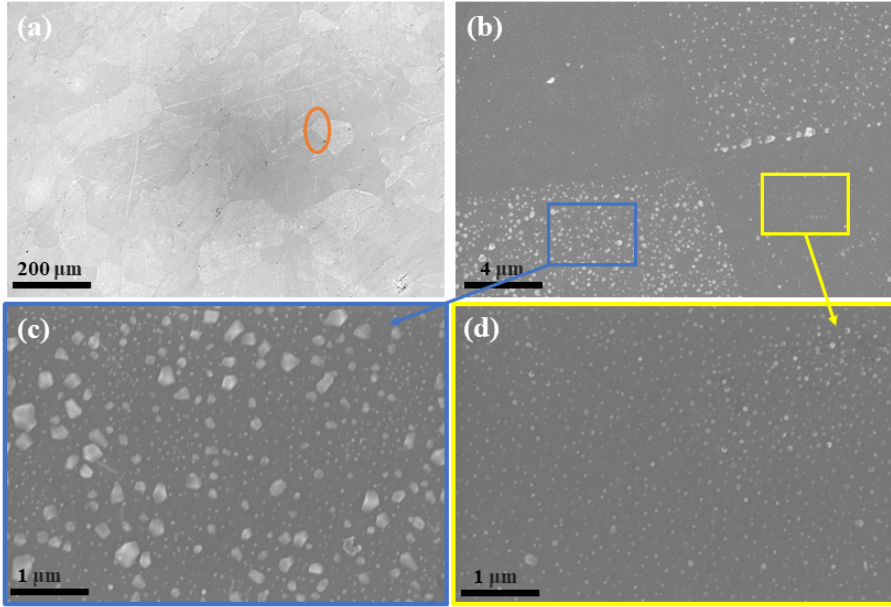


Fig. 2. (Color online) Non-uniform distribution of tin sites on EP fine-grain surface. (a) bright and dark areas corresponding to regions with higher and lower nuclei density, (b) junction of bright and dark areas at higher magnification, (c) and (d) show details for the selected areas in (b).

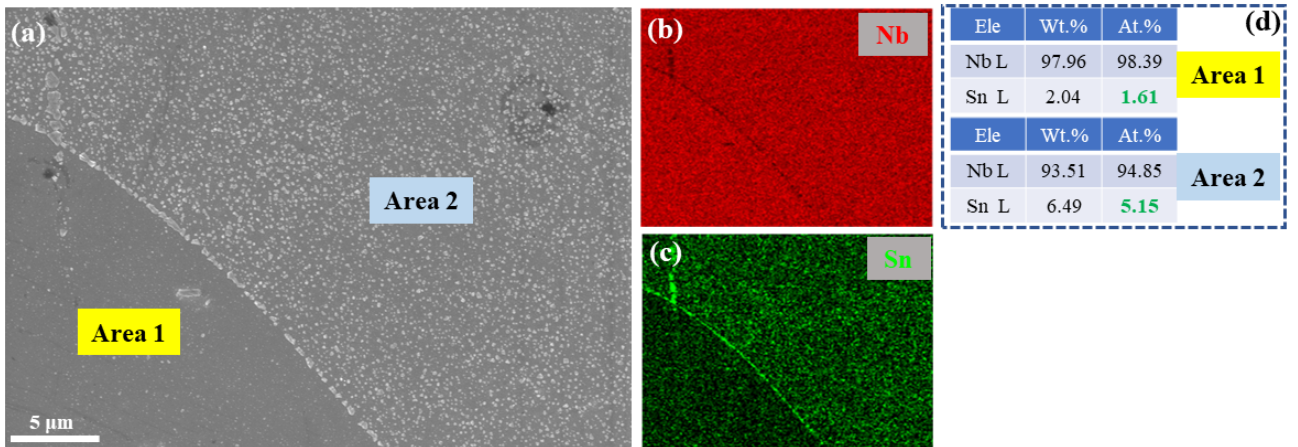


Fig. 3. (Color online) Microstructures and elemental distribution of tin on bright and dark areas. (a) the topography of the interface region, (b) and (c) distribution of Nb and Sn of this region respectively, (d) specific element content is given for Area 1 and 2 in (a).

relation between nucleation density and orientation more directly, a series of large-grain samples with a singular orientation were prepared to observe and analyze the nucleation behavior. Fig. 4b-d depict the nucleation behavior of Nb (100), Nb (110), and Nb (211) under identical nucleation conditions, respectively. The analysis clearly indicates that the density of the tin nuclei on the Nb (100) crystal plane is notably greater than that observed in the other two crystal planes. However, owing to the lower spatial resolution of EDS, no obvious difference in the tin content on the three crystal surfaces was observed. Hence, AES and SAXPS techniques were utilized to effectively discern the disparity in tin content among the three crystal planes under consideration. The results are pre-

sented in Table 1. These findings indicate that the density of the tin nuclei on the Nb (100) surface is greater than that on the Nb (110) and Nb (211) surfaces.

B. Relationship Between Grain Orientation and tin nuclei Density

Despite the obvious observation of large differences in the density and morphology of tin nuclei on distinct grain surfaces of BCP Nb samples, the high surface roughness prevents the use of EBSD to determine the relationship between grain orientation and nucleation behavior. In addition, the

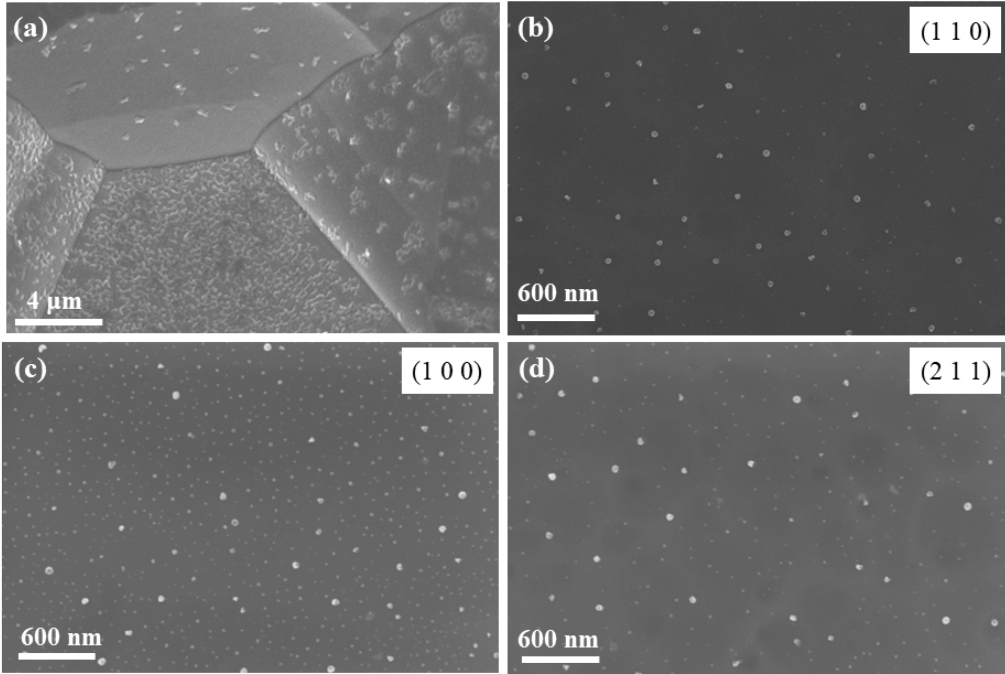


Fig. 4. (Color online) (a) Non-uniform distribution of tin sites on the BCP fine-grain surface which examines the relationship between nucleation behavior and grain orientation, (b), (c) and (d) correspond to large-grain Nb (110), Nb (100), and Nb (211) respectively.

Table 1. AES and SAXPS results of the relative content of tin on large-grain Nb (110), Nb (100), and Nb (211) respectively.

Crystal plane	AES			SAXPS		
	(100)	(110)	(211)	(100)	(110)	(211)
Sn content (at%)	4.8	3.6	4.8	13.7	5.3	6.3
Nb content (at%)	6.7	7.0	8.3	10.9	9	6.6
Sn / (Nb + Sn) %	41.7	34.0	36.6	55.7	37.1	48.8

nucleation characteristics of the large-grain niobium surface were not as significant as those of the fine-grain surface. The underlying cause of this phenomenon was elucidated in III D. In contrast, the surface condition of EP samples not only meets the requirements of EBSD but also reflects the difference in nucleation behavior between orientations. During the nucleation process, SnCl_2 was selectively adsorbed in distinct orientations, and the size of the bright and dark areas on the surface of the EP samples were consistent with the grain size of niobium.

To validate the aforementioned hypothesis, EBSD analysis was conducted on the surface of the EP samples to establish the correlation between grain orientation and tin nuclei density. The results of the analysis are shown in Fig. 5. Fig. 5a and Fig. 5c show the microscopic topography, which exhibits distinct bright and dark zones of interest. The bright and dark areas correspond to the different densities of tin nuclei mentioned above. Fig. 5b and Fig. 5d depict a typical EBSD In-

verse Pole Figure (IPF) coloration orientation map for Fig. 5a and Fig. 5c, which contain dozens of grains with sizes ranging from tens to hundreds of microns. The IPF exhibited approximately eight total discernible orientations. Notably, a recurring phenomenon was detected in both sets of IPF images. The bright regions correlate to grains with specific orientations. The bright areas observed during the nucleation stage can be attributed to the enhanced adsorption of tin nuclei by Nb (100), Nb (310), and Nb (311). In contrast, the surfaces of Nb (110), Nb (111), Nb (221), Nb (321), and Nb (211) exhibited fewer adsorbed tin nuclei, leading to the formation of black regions when observed in the secondary electron mode. In addition, a comprehensive examination of the surface was conducted using EBSD analyses. The findings obtained from these analyses exhibit a high degree of agreement with the outcomes depicted in Fig. 5. This correspondence suggests a robust association between nucleation behavior and grain orientation. Significantly, the conclusion derived from the aforementioned experiments aligns well with the findings obtained from the large-grain samples, indicating that SnCl_2 exhibits a higher affinity for adsorption on the surface of Nb (100) than Nb (110) and Nb (211).

Previous studies suggest that the observed behavior can be attributed to the varying adsorption capacities exhibited by each crystal plane. The adsorption anisotropy is attributed to changes in the adsorption energy of SnCl_2 on distinct crystal surfaces. Through a combination of experimental and simulation approaches, Morris et al. demonstrated that various crystal facets of metals exhibit unique adsorption capabilities. For instance, the likelihood of nitrogen molecules ad-

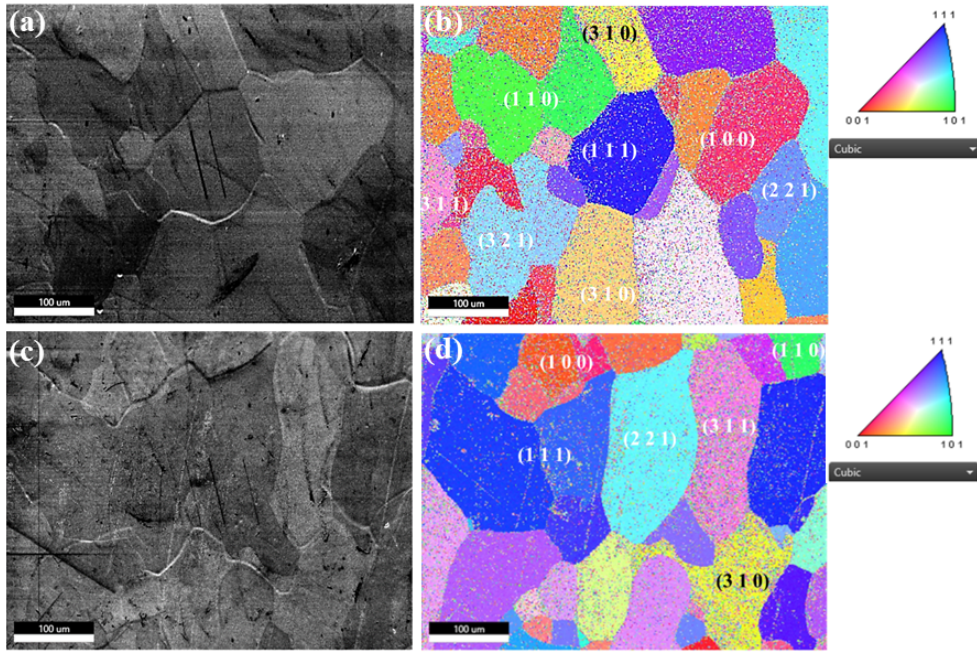


Fig. 5. (Color online) (a) and (c) show the microscopic topography of nucleation surface containing several bright and dark regions, (b) and (d) correspond to the EBSD IPF coloring orientation map for (a) and (c), respectively.

hering to W (320) is 0.7, whereas the adhesion probability to W (110) is significantly lower at 3×10^{-3} , as discussed in the literature [52]. Furthermore, a study conducted by Pal et al. revealed that the adsorption capacity of isoctylphenoxy polyethoxyethanol molecules on Si (110) is significantly higher than that on Si (100) when exposed to a liquid environment. This disparity in the adsorption strength was utilized to control the chemical polishing rate of silicon crystals with various orientations [53]. Additionally, Hirai et al. [54] developed a high-precision, fast-response, and high-performance chemical sensor based on the fact that various surfaces have distinct adsorption capacities for gas molecules, thereby achieving rapid detection of gas species. It is evident that the crystal planes exhibited noticeable variations in their adsorption capacities under both vacuum and liquid conditions. The results of the nucleation experiments conducted on EP fine-grain and large-grain samples consistently demonstrate that the non-uniform distribution of tin nuclei on the niobium surface is caused by the selective adsorption of SnCl_2 molecules on different crystal planes. Furthermore, these experiments established a qualitative relationship between adsorption capacity and various orientations. Subsequently, we ascertained the accuracy of this mechanism by conducting simulations to evaluate the adsorption capability of SnCl_2 molecules on various crystal planes.

C. Structural and adsorption properties of SnCl_2 on different crystal planes by DFT simulations

To enhance the validity of the EBSD analysis, we performed calculations to determine the adsorption energy on several crystal planes, namely Nb (110), Nb (100), Nb (211), Nb (111), Nb (221), Nb (310), Nb (311), and Nb (321), as indicated by the EBSD and XRD findings. The adsorption capacity of solitary tin and chlorine atoms on the Nb surface were calculated to determine the most stable adsorption sites. Three adsorption sites with high symmetry, namely the top site (T), hollow site (H), and bridge site (B), were studied. The calculations indicated a notable preference for tin atoms to adsorb on the hollow site, whereas chlorine atoms exhibited a clear tendency to adsorb on the bridge site.

Subsequently, computational analysis of the adsorption of SnCl_2 molecules in different orientations was performed. Two distinct molecular configurations, one with upright molecules and the other with molecules lying down, were examined. In both configurations, the tin atom was positioned closer to the surface. The adsorption sites and their corresponding configurations are shown in Fig. 6. The final stable adsorption configuration of SnCl_2 on the surface was observed to be lying-down with the Sn atom occupying a hollow position, regardless of the initial configuration. The adsorption energies of each orientation under this configuration are presented in Table 2. When the computed adsorption energy is negative, the reaction is characterized by exothermicity and the adsorption site can be considered stable. Conversely, a positive adsorption energy implies an endothermic adsorption process and unstable adsorption site.

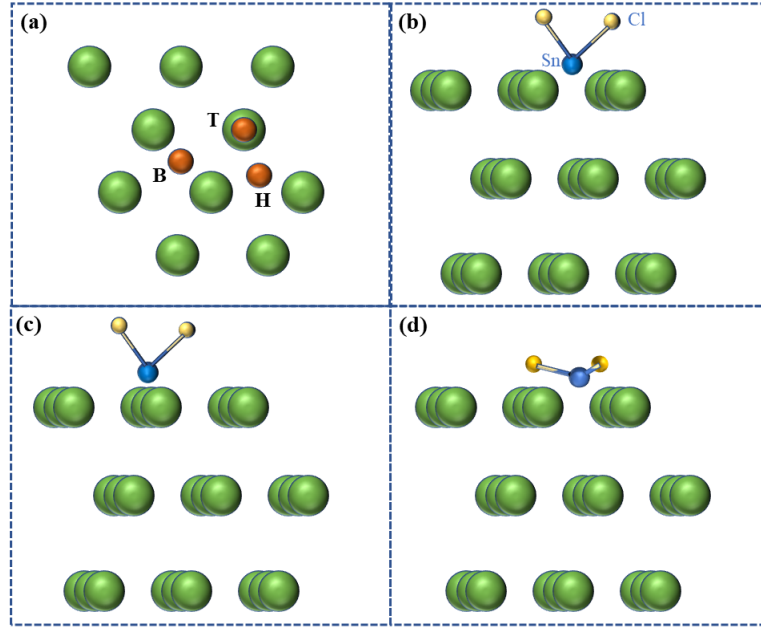


Fig. 6. (Color online) The adsorption sites and adsorption geometries of SnCl₂ on the Nb surface. (a) shows various adsorption sites from the top view, (b) shows the side view of upright SnCl₂ adsorption on hollow or bridge sites, (c) corresponds to adsorption on the top site when SnCl₂ is upright, (d) shows lying-down the adsorption condition when SnCl₂ is lying-down.

Table 2. Adsorption energies of SnCl₂ molecules on various orientations of Nb surface.

E _{SnCl₂} (eV)	E _{clean} (eV)	E _{SnCl₂/Nb} (eV)	E _{ads} (eV)
-2907.001	E ₍₁₁₀₎	-165703.61	E _{SnCl₂/(110)} -168616.57
	E ₍₁₀₀₎	-59634.07	E _{SnCl₂/(100)} -62548.30
	E ₍₃₁₀₎	-74529.32	E _{SnCl₂/(310)} -77459.68
	E ₍₂₁₁₎	-74546.26	E _{SnCl₂/(211)} -77459.68
	E ₍₁₁₁₎	-74523.19	E _{SnCl₂/(111)} -77436.01
	E ₍₂₂₁₎	-149065.87	E _{SnCl₂/(221)} -151979.60
	E ₍₃₁₁₎	-149049.36	E _{SnCl₂/(311)} -151963.22
	E ₍₃₂₁₎	-89436.84	E _{SnCl₂/(321)} -92349.31

The adsorption energy was negative in all cases, indicating the exothermic nature of the adsorption process. The orientation of SnCl₂ with the tin atom located on the hollow site was calculated to be the most stable of all the possible orientations. This is attributed to the fact that the vertical distance between SnCl₂ and the surface is the shortest in this orientation. Additionally, a positive correlation between the vertical adsorption heights and adsorption energies was observed. In other words, a lower adsorption energy corresponded to a higher adsorption height. Furthermore, upon optimization, the initial configurations featuring horizontal SnCl₂ adsorption on the top and bridge sites transitioned to a configuration in which SnCl₂ was adsorbed horizontally on the hollow sites. This suggests that the lying-down structure represents

the most thermodynamically stable adsorption configuration and is aligned with the single-atom adsorption structure. Furthermore, it is worth noting that the extended Sn-Cl bond is consistently observed in all instances. Additionally, the Sn-Cl distance of SnCl₂ when adsorbed on the hollow site was greater than that on the top and bridge sites, which agrees well with the results obtained for the adsorption energy.

The adsorption energies of SnCl₂ on various crystal surfaces were determined using the above Equation , and the results are presented in Table 2. The data shown in Table 2 demonstrates that the SnCl₂ molecule has a favorable tendency to adsorb onto the Nb (100), Nb (310), and Nb (311) surfaces, as evidenced by the adsorption energy values of -7.23 eV, -6.55 eV, and -6.86 eV, respectively. The

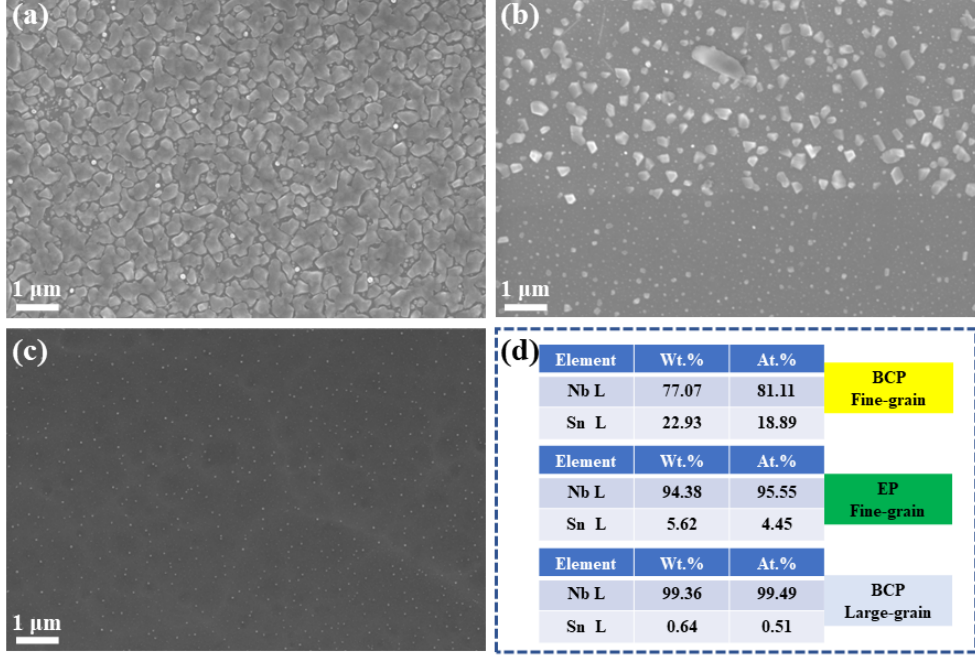


Fig. 7. (Color online) (a), (b), and (c) correspond to nucleation behavior on the BCP fine-grain surface, EP fine-grain surface, and BCP large-grain surface, (d) specific element content of (a), (b), and (c).



Fig. 8. (Color online) A schematic diagram illustrating the adsorption behavior of the surface with different morphology, where the density of steps reflects the surface roughness.

adsorption capacities of the Nb (111), Nb (110), and Nb (321) surfaces were comparatively low in strength, as indicated by the adsorption energies of -5.82 eV , -5.95 eV , and -5.47 eV , respectively. Significantly, the simulated outcomes pertaining to the adsorption capability of the SnCl_2 molecule on various crystal orientations exhibited commendable concurrence with the observed preferred adsorption phenomena in the nucleation studies, as determined by EBSD analysis.

D. Effect of surface roughness and grain boundary on nucleation behavior

Furthermore, notable variations in the nucleation behavior were observed across the BCP, EP fine-grain, and BCP large-grain samples when subjected to identical nucleation condi-

tions, as depicted in Fig. 7. In contrast to the EP treatment, the surface state of BCP exhibited greater fluctuations, leading to increased surface roughness. It is worth noting that BCP selectively dissolves the surface of Nb. Owing to the difference in energy between the different crystal planes, the dissolution rate of Nb (100) is the slowest, whereas Nb (110) and Nb (111) dissolve faster, resulting in a dominant grain orientation of Nb (100) on the BCP fine-grain surface [55, 56]. In contrast, the dissolution of the EP Nb surface is more strongly dependent on the current density distribution, thus leading to a more random grain orientation distribution on the EP fine-grain surface without a clear preferred orientation [57]. Based on our experiments and DFT simulation findings, Nb (100) is more favorable for the formation of tin nuclei during the nucleation stage. Therefore, the rough surface resulting from the BCP offers more Nb (100), which is beneficial for the adsorption of tin nuclei compared to the smooth surface produced by

the EP. However, it is crucial to highlight that the tin (Sn) content of approximately 18.89% present on the surface of the fine crystal BCP is notably higher than the 1%-6% content found on the surface of EP under identical nucleation conditions. Consequently, the influence of surface roughness on nucleation is evident and holds significant importance. This finding suggests that the geometric and morphological characteristics of the surface have a significant impact on the nucleation behavior. Consistent with the phenomenon observed by Zhang et al. [58], the nucleation experiment demonstrates that the density of the nucleation sites decreases substantially with decreasing substrate roughness. In addition, the presence of a significant amount of tin on the surface of BCP fine-grain samples obscures the occurrence of an uneven distribution of tin nuclei and hence the infrequent observation of a non-uniform distribution in BCP samples during the initial stage. In addition, by comparing the nucleation behaviors of the fine- and large-grain samples, an intriguing phenomenon was identified: the nucleation density of the large-grain samples was relatively low, which may be ascribed to fewer grain boundaries or a smoother surface. Based on the aforementioned experimental findings, morphology should be acknowledged as a significant determinant of the nucleation behavior. The increased density of tin nuclei observed in the BCP samples can be attributed to the more frequently occurring fluctuations at the interface, thereby facilitating favorable nucleation conditions, as depicted in Fig. 8. This observation aligns with the conclusion of Yuan et al., who posited that steps provide a greater number of binding sites and exhibit higher diffusion barriers than terraces [59]. Moreover, the significant difference in the nucleation behavior between the fine- and large-grain samples suggests that the number of grain boundaries may also influence nucleation behavior. The influence of the number of grain boundaries on nucleation behavior can be attributed to the presence of lattice distortion at the interfaces between grains, which results in an elevated energy state at these locations compared to the energy within the grains themselves. Consequently, the surfaces with

a greater number of grain boundaries are more likely to satisfy the nucleation criterion. However, samples with larger grain sizes exhibited reduced surface roughness following polishing. This can be attributed to the presence of fewer grain boundaries, which subsequently decreases the density of tin nuclei during the nucleation process.

IV. CONCLUSION

This study examined the nucleation behavior of tin nuclei during the growth process of Nb_3Sn thin films on an Nb surface utilizing a SnCl_2 agent and vapor diffusion method.

1. The nonuniform distribution of tin nuclei on the surface of Nb was observed through experimental investigation and material characterization. Furthermore, the correlation between the nonuniformity and orientation of the Nb grains was validated.

2. The adsorption energy of SnCl_2 molecules on the surfaces of Nb grains with varying orientations was determined using DFT simulations. These findings indicate that the uneven dispersion of the tin nuclei can be attributed to variations in the adsorption energy of SnCl_2 molecules across different grain orientations.

3. The investigation of large crystalline niobium substrates has provided additional evidence supporting the significant influence of surface morphology and grain size on the nucleation behavior. Moreover, a potential mechanism was proposed to explain these observations.

The research conducted in this study presents valuable insights for enhancing and optimizing the surface pretreatment procedure of Nb with the aim of achieving a uniform distribution of tin nuclei in accordance with specific specifications.

V. BIBLIOGRAPHY

- [1] X.Y. Pu, H.T. Hou, Y. Wang et al., Frequency sensitivity of the passive third harmonic superconducting cavity for SSRF. *Nucl. Sci. Tech.* **31**, 3 (2020). doi: [10.1007/s41365-020-0732-x](https://doi.org/10.1007/s41365-020-0732-x)
- [2] P.P. Gong, Y.B. Zhao, H.T. Hou et al., Tuning control system of a third harmonic superconducting cavity in the Shanghai Synchrotron Radiation Facility. *Nucl. Sci. Tech.* **30**, 157 (2019). doi: [10.1007/s41365-019-0669-0](https://doi.org/10.1007/s41365-019-0669-0)
- [3] P. Kneisel, Superconducting Radio Frequency Technology: An Overview. *Mater. Tech.* **91**, 7–12 (2003). doi: [10.1051/MAT-TECH/200391070007](https://doi.org/10.1051/MAT-TECH/200391070007)
- [4] P. Sha, W.M. Pan, S. Jin et al., Ultrahigh accelerating gradient and quality factor of CEPC 650MHz superconducting radio-frequency cavity. *Nucl. Sci. Tech.* **33**, 1–8 (2022). doi: [10.1007/s41365-022-01109-8](https://doi.org/10.1007/s41365-022-01109-8)
- [5] P. Sha, J.K. Hao, W.M. Pan et al., Nitrogen doping/infusion of 650 MHz cavities for CEPC. *Nucl. Sci. Tech.* **32**, 45 (2021). doi: [10.1007/s41365-021-00881-3](https://doi.org/10.1007/s41365-021-00881-3)
- [6] R.A. Briere, F.A. Harris, R.E. Mitchell, Physics Accomplish- ments and Future Prospects of the BES Experiments at the BEPC Collider. *Annu. Rev. Nucl. Part. Sci.* **66**, 143–170 (2021). doi: [10.1146/annurev-nucl-102115-044802](https://doi.org/10.1146/annurev-nucl-102115-044802)
- [7] H.J. Zheng, J. Gao, J.Y. Zhai et al., RF design of 650-MHz 2-cell cavity for CEPC. *Nucl. Sci. Tech.* **30**, 155 (2019). doi: [10.1007/s41365-019-0671-6](https://doi.org/10.1007/s41365-019-0671-6)
- [8] Y.X. Zhang, J.F. Chen, D. Wang, RF design optimization for the SHINE 3.9 GHz cavity. *Nucl. Sci. Tech.* **31**, 73 (2020). doi: [10.1007/s41365-020-00772-z](https://doi.org/10.1007/s41365-020-00772-z)
- [9] N.S. Huang, Z.P. Liu, B.J. Deng, The MING proposal at SHINE: megahertz cavity enhanced X-ray generation. *Nucl. Sci. Tech.* **34**, 6 (2023). doi: [10.1007/s41365-022-01151-6](https://doi.org/10.1007/s41365-022-01151-6)
- [10] M.X. Xu, Y. He, S.X. Zhang et al., Low beta superconducting cavity system design for HIAF iLinac. *Nucl. Eng. Technol.* **55**, 2466–2473 (2023). doi: [10.1016/j.net.2023.04.010](https://doi.org/10.1016/j.net.2023.04.010)
- [11] X.F. Niu, F. Bai, X.J. Wang et al., Cryogenic system design for HIAF iLinac. *Nucl. Sci. Tech.* **30**, 178 (2019). doi: [10.1007/s41365-019-0700-5](https://doi.org/10.1007/s41365-019-0700-5)

[12] F. Yan, H.P. Geng, C. Meng et al., Commissioning experiences with the spoke-based CW superconducting proton linac. *Nucl. Sci. Tech.* **32**, 105 (2021). [doi: 10.1007/s41365-021-00950-7](https://doi.org/10.1007/s41365-021-00950-7)

[13] F. Furuta, K. Saeki, T. Saeki et al., Experimental comparison at KEK of high gradient performance of different single cell superconducting cavity designs, in *Proceedings of IPAC2006*.

[14] G.V. Eremeev, R.L. Geng, H. Padamsee et al., High gradient studies for ILC with single-cell re-entrant shape and elliptical shape cavities made of fine-grain and large-grain niobium, in *Proceedings of IEEE Particle Accelerator Conference*, (2007), pp. 4093

[15] S. Posen, Understanding And Overcoming Limitation Mechanisms In Nb₃Sn Superconducting RF Cavities, PhD thesis, Cornell University, (2015)

[16] S. Norihiro, H.S. Zen, O. Hideaki, Measurement of bunch length evolution in electron beam macropulse of S-band linac using coherent edge radiation. *Phys. Lett. A.* **383**, 5 (2018). [doi: 10.1016/j.physleta.2018.11.010](https://doi.org/10.1016/j.physleta.2018.11.010)

[17] B.J. Patil, S.T. Chavan, S.N. Pethe et al., Design of 6 Mev linear accelerator based pulsed thermal neutron source: FLUKA simulation and experiment. *Appl. Radiat. Isot.* **70**, 149–155 (2012). [doi: 10.1016/j.apradiso.2011.08.019](https://doi.org/10.1016/j.apradiso.2011.08.019)

[18] Radiation treatment of gaseous and liquid effluents for contaminant removal, in *proceedings of a technical meeting held in Sofia*, Bulgaria (2004)

[19] A. Pramudita, Linacs for Medical Isotope Production. *At. Indones.* **37**, 391–399 (2011). [doi: 10.17146/aij.2011.68](https://doi.org/10.17146/aij.2011.68)

[20] S.K. Chen, Y.C. Yang, D.Z. Guo, Study on the area ratio of Nb–Sn target for the preparation of Nb₃Sn films. *Radiation Detection Technology and Methods* **3** 54 (2019). [doi: https://doi.org/10.1007/s41605-019-0134-y](https://doi.org/10.1007/s41605-019-0134-y)

[21] E.A. Llyina, G. Rosaz, J.B. Descarrega et al., Development of sputtered Nb₃Sn films on copper substrates for superconducting radiofrequency applications. *Supercond. Sci. Technol.* **32**, 3 (2019). [doi: 10.1088/1361-6668/aaf61f](https://doi.org/10.1088/1361-6668/aaf61f)

[22] W.W. Tan, R. Ma, H. Pan et al., The observation of tin islands in Nb₃Sn thin films deposited by magnetron sputtering. *Phys. C* **576**, 1353667 (2020). [doi: 10.1016/j.physc.2020.1353667](https://doi.org/10.1016/j.physc.2020.1353667)

[23] S.M. Deambrosis, A.A. Rossia, V. Ruppa et al., A15 superconductors by thermal diffusion in 6 GHz cavities, in *Proceedings of SRF 2019*, Berlin, Germany (2009)

[24] R.H. Hammond, Synthesis and physical properties of superconducting compound films formed by the electron-beam codeposition of the elements. *J. Vac. Sci. Technol.* **15**, 382–385 (1978). [doi: 10.1116/1.569552](https://doi.org/10.1116/1.569552)

[25] P.G. Kosky, H.C. Peters, C.L. Spiro et al., Superconducting Nb₃Sn joints by chemical vapour deposition. *Cryogenics* **35**, 77 (1995). [doi: 10.1016/0011-2275\(94\)90162-7](https://doi.org/10.1016/0011-2275(94)90162-7)

[26] E. Barzi, M. Bestetti, F. Reginato et al., Synthesis of superconducting Nb₃Sn coatings on Nb substrates. *Supercond. Sci. Technol.* **29**, (2016). [doi: 10.1088/0953-2048/29/1/015009](https://doi.org/10.1088/0953-2048/29/1/015009)

[27] L. Zhu, X.Y. Lu, Z.Q. Yang et al., Study on preparation of Nb₃Sn films by bronze route. *Phys. C.* **601**, 1354113 (2022). [doi: 10.1016/j.physc.2022.1354113](https://doi.org/10.1016/j.physc.2022.1354113)

[28] M. Lu, D.D. Luo, F. Pan et al., Development and performance of the first Nb₃Sn thin-film cavity via bronze process. *Chin. Phys. Lett.* **39**, 115201 (2022). [doi: 10.1088/0256-307X/39/11/115201](https://doi.org/10.1088/0256-307X/39/11/115201)

[29] F. Pan, M. Lu, A.D. Wu et al., Structural and superconducting properties of Nb₃Sn film for superconducting radio-frequency cavities synthesized via bronze route. *Funct. Mater. Lett.* **14**, 2151030 (2021). [doi: 10.1142/s1793604721510309](https://doi.org/10.1142/s1793604721510309)

[30] U. Pudasaini, G.V. Eremeev, C. Grigory et al., Initial growth of tin on niobium for vapor diffusion coating of Nb₃Sn. *Supercond. Sci. Technol.* **32**, 4 (2018). [doi: 10.1088/1361-6668/aa8a88](https://doi.org/10.1088/1361-6668/aa8a88)

[31] G.Z. Jiang, S. Wu, Z.Q. Yang et al., Understanding and optimization of the coating process of the radio-frequency Nb₃Sn thin film superconducting cavities using tin vapor diffusion method. *Appl. Surf. Sci.* **643**, 158708 (2024). [doi: 10.1016/j.apsusc.2023.158708](https://doi.org/10.1016/j.apsusc.2023.158708)

[32] G. Wang, S.W. Quan, L. Lin et al., Nb₃Sn cavities coated by tin vapor diffusion method at Peking University. *Appl. Sci.* **13**, 15 (2023). [doi: 10.3390/app13158618](https://doi.org/10.3390/app13158618)

[33] C. Dong, Z.F. Lin, P. Sha et al., Preliminary research of niobium cavity coating with Nb₃Sn film at IHEP. *Physica. C* **600**, 1354107 (2023). [doi: 10.1016/j.physc.2022.1354107](https://doi.org/10.1016/j.physc.2022.1354107)

[34] X.Q. Jia, Method for growing Nb₃Sn films at fast speed and low cost. *Sci. Technol.* **34**, 100501 (2021). [doi: 10.1088/1361-6668/ac1e66](https://doi.org/10.1088/1361-6668/ac1e66)

[35] U. Pudasaini, G. Eremeev, C. E. Reece et al., Recent results from Nb₃Sn single cell cavities coated at Jefferson lab, in *Proceedings of SRF 2019*, Dresden, Germany (2023)

[36] B. Hillenbrand, H. Martens, H. Pfister et al., Superconducting Nb₃Sn cavities with high microwave qualities. *IEEE Trans. Magn.* **13**, 491–495 (1977). [doi: 10.1109/T-MAG.1977.1059299](https://doi.org/10.1109/T-MAG.1977.1059299)

[37] U. Pudasaini, Growth and properties of vapor diffused Nb₃Sn coating for superconducting radiofrequency accelerator cavity applications, PhD thesis, The College of William and Mary, (2020)

[38] M. Peiniger, M. Hein, N. Klein et al., Work on Nb₃Sn Cavities at Wuppertal, in *Proceedings of The Third Workshop on RF Superconductivity*, Illinois, USA (1987)

[39] D. Hall, New insights into the limitations on the efficiency and achievable gradients in Nb₃Sn SRF cavities, PhD thesis, Cornell University, (2017)

[40] U. Pudasaini, Overview of Nb₃Sn cavity technology development for Jefferson Lab, in *Proceedings of 10th Workshop on thin films and new ideas for pushing the limits of RF superconductivity*, (2022)

[41] U. Pudasaini, C.E. Reece, J.K. Tiskumara, Managing Sn-Supply to tune surface characteristics of vapor-diffusion coating of Nb₃Sn. (2022). [doi: 10.18429/JACoW-SRF2021-TUPTEV013](https://doi.org/10.18429/JACoW-SRF2021-TUPTEV013)

[42] S. Posen, J. Lee, D. Seidman et al., Advances in Nb₃Sn superconducting radiofrequency cavities towards first practical accelerator applications. *Supercond. Sci. Technol.* **34**, 025007 (2021). [doi: 10.1088/1361-6668/abc7f7](https://doi.org/10.1088/1361-6668/abc7f7)

[43] Q.Y. Shao, R.C. Fang, G.Z. Wang et al., Growth evolution of thin films from vapor: The role of small mobility clusters at the nucleation stage. *Prog. Cryst. Growth Charact. Mater.* **40**, 221–225 (2000). [doi: 10.1016/S0960-8974\(00\)00036-X](https://doi.org/10.1016/S0960-8974(00)00036-X)

[44] J. Cardoso, M. Harsdorfe, Influence of surface defects on heterogeneous nucleation and growth of thin-films. *Zeitschrift für Naturforschung A* **33**, 442–446 (1978). [doi: 10.1515/zna-1978-0407](https://doi.org/10.1515/zna-1978-0407)

[45] J.A. Zhou, J.H. Wang, R.Z. Yuan et al., The effect of diamond film nucleation and growth in different substrate pretreatment methods. *Eng. J.* **14**, 48–52 (1999).

[46] C.J. Tang, A.J. Neves, A. Fernandes, Influence of nucleation density on film quality, growth rate and morphology of thick CVD diamond films. *Diamond Relat. Mater.* **12**, 1488–1494 (2003). [doi: 10.1016/S0925-9635\(03\)00179-1](https://doi.org/10.1016/S0925-9635(03)00179-1)

[47] E.N. Popova, I.L. Deryagina, E.G. Valova-Zakharevskaya et al., Effect of annealing regimes on the structure of Nb₃Sn su-

superconducting layers in composites with Internal Tin sources. *Phys. Met. and Metallogr.* **117**, 1028–1037 (2016). [doi: 10.1134/S0031918X16100082](https://doi.org/10.1134/S0031918X16100082)

[48] E.N. Popova, I.L. Deryagina, Optimization of the microstructure of Nb₃Sn layers in superconducting composites. *Phys. Met. and Metallogr.* **119**, 1229–1235 (2018). [doi: 10.1134/S0031918X18120153](https://doi.org/10.1134/S0031918X18120153)

[49] I.L. Deryagina, E.N. Popova, E.G. Zaharevskaya et al., Effect of Doping Mode and Composite Geometry on the Structure of Nanocrystalline Nb₃Sn Layers in Superconducting Nb/Cu-Sn Composites. *J. Sib. Fed. Univ.* **4**, 149–161 (2011).

[50] Z.Q. Yang, Y. He, F. Pan, Several experimental phenomena of Sn nucleation on Nb surface observed at IMP, in *Proceedings of LINAC2018*, Beijing, China (2018). [doi: 10.18429/JACoW-LINAC2018-TUPO038](https://doi.org/10.18429/JACoW-LINAC2018-TUPO038)

[51] S. Wu, Z.Q. Yang, Y. He et al., The mechanism of nonuniform distribution of tin sites on the surface of niobium, in *Proceedings of IPAC2023*, Venice, Italy (2023). [doi: 10.18429/JACoW-IPAC2023-WEPA170](https://doi.org/10.18429/JACoW-IPAC2023-WEPA170)

[52] M.A. Morris, M. Bowker, D.A. King, Kinetics of Adsorption, Desorption and Diffusion at Metal Surfaces. *Comprehensive Chemical Kinetics* **19**, 1–179 (1984). [doi: 10.1016/S0069-8040\(08\)70099-2](https://doi.org/10.1016/S0069-8040(08)70099-2)

[53] P. Pal, K. Sato, M.A. Gosalvez et al., Surfactant Adsorption on Single-Crystal Silicon Surfaces in TMAH Solution: Orientation-Dependent Adsorption Detected by in-situ Infrared Spectroscopy. *J. Microelectromech. Syst.* **18**, 1345–1356 (2009). [doi: 10.1109/JMEMS.2009.2031688](https://doi.org/10.1109/JMEMS.2009.2031688)

[54] K. Hirai, K. Sumida, M. Meilikov et al., Impact of crystal orientation on the adsorption kinetics of a porous coordination polymer–quartz crystal microbalance hybrid sensor. *J. Mater. Chem. C* **2**, 3336–3344 (2014). [doi: 10.1039/C3TC32101K](https://doi.org/10.1039/C3TC32101K)

[55] T. Hui, E.R. Charles, J.K. Michael et al., Surface studies of niobium chemically polished under conditions for superconducting radio frequency (SRF) cavity production. *Appl. Surf. Sci.* **253**, 1236–1242 (2006). [doi: 10.1016/j.apsusc.2006.01.083](https://doi.org/10.1016/j.apsusc.2006.01.083)

[56] Z.H. Sung, A. Dzyuba, P.J. Lee et al., Evidence of incomplete annealing at 800 °C and the effects of 120 °C baking on the crystal orientation and the surface superconducting properties of cold-worked and chemically polished Nb. *Supercond. Sci. Technol.* **28**, 075003 (2015). [doi: 10.1088/0953-2048/28/7/075003](https://doi.org/10.1088/0953-2048/28/7/075003)

[57] N.M. Khun, M. Sumption, G.S. Frankel, Smoothening of niobium by electropolishing. *J. Appl. Electrochem.* **43**, 829–838 (2013). [doi: 10.1007/s10800-013-0574-x](https://doi.org/10.1007/s10800-013-0574-x)

[58] Y. Zhang, M. Wang, X. Lin et al., Effect of substrate surface microstructure on heterogeneous nucleation behavior. *J. Mater. Sci. Technol.* **28**, 67–72 (2012). [doi: 10.1016/S1005-0302\(12\)60025-5](https://doi.org/10.1016/S1005-0302(12)60025-5)

[59] Y. Yuan, D. Zhang, F.H. Zhang et al., Crystallographic orientation dependence of nanopattern morphology and size in electropolished polycrystalline and monocrystalline aluminum: an EBSD and SEM Study. *J. Electrochem. Soc.* **167**, 113505 (2020). [doi: 10.1149/1945-7111/aba6c7](https://doi.org/10.1149/1945-7111/aba6c7)